Room-Temperature Fabrication of Garnet-Type Solid-Electrolyte: Optimizing Particle Size for High Ionic Conductivity

Jinhyup Han [a,c], Anh Vu [a], Jae Jin Kim [a], Jihyeon Gim [a,], Jason R. Croy [a], Tae H. Lee [b,*], and Eungje Lee [a,*]*

[a] Chemical Sciences and Engineering Division, Argonne National Laboratory, Lemont, IL 60439, USA

[b] Applied Materials Division, Argonne National Laboratory, Lemont, IL 60439, USA

[c] Department of Chemical Engineering, Keimyung University, Daegu 42601, S. Korea

*Corresponding authors: eungje.lee@anl.gov, thlee@anl.gov, jgim@anl.gov

Keywords: Garnet, $Li_7La_3Zr_2O_{12}$ (LLZO), Aerosol deposition, Solid electrolyte

Abstract

Dense and uniform $Li_{6.25}Al_{0.25}La_3Zr_2O_{12}$ (Al-doped LLZO) solid-electrolyte film of ~24 μm thickness is successfully fabricated by room temperature aerosol deposition (AD) method. The process optimization study revealed that careful control of particle size and morphology is one of critical determinants in the development of a compact AD membrane. Notably, our method facilitated an impressive ionic conductivity of approximately 10^{-5} S cm^{-1}, bypassing the necessity for post-annealing processes, a milestone in itself. However, it is hypothesized that the attained conductivity is somewhat restrained by factors such as smaller grain size and potential surface degradation due to moisture exposure during fabrication, indicating avenues for further research. Looking forward, detailed investigations into the film's microstructure and its impact on transport properties will be a focal point, alongside potential enhancements through post-annealing and particle coating strategies. This research hints at a promising trajectory for the development of high-efficiency solid-state battery technology.

1. Introduction

All-solid-state batteries (ASSBs) have emerged as a compelling area of research and development due to their potential to address the safety issues associated with the flammable organic liquid electrolytes in traditional Li-ion batteries [1-3]. Of the various solid electrolytes (SEs) under consideration, oxide-based SEs like the garnet-structured $Li_7La_3Zr_2O_{12}$ (LLZO) are especially promising. LLZO has two phases: tetragonal and cubic phases. The cubic phase has higher ionic conductivity compared to the tetragonal phase. However, producing a pure cubic LLZO phase at room temperature is a significant challenge, as the tetragonal phase tends to form more stably at a low temperature. To stabilize the cubic phase, various doping elements have been explored, including Al, Ta, Ga, Nb, and others. Among these, Al has emerged as a prominent doping element due to its low cost and ability to enhance ionic conductivity effectively. [4, 5]. The Al-doped LLZO (Al-LLZO) solid electrolytes offer high ionic conductivity (10^{-3} to 10^{-4} S cm^{-1}) and exhibit a broad electrochemical stability window, permitting the use of high-voltage cathodes and Li metal anodes to achieve high-energy-density batteries [6, 7].

Despite these advantages, challenges persist, impeding the practical adoption of oxide-based SEs. Primary concerns include high interfacial resistance with electrodes, suboptimal mechanical properties, and the complexities of scaling up manufacturing [8, 9]. In addition, Li/garnet LLZO high interfacial resistance is still a challenge due to lithiophobic Li_2CO_3 impurities at the garnet surface [10, 11]. Standard ceramic processing for materials like LLZO entails steps such as powder compaction, shape forming, binder removal, and high-temperature densification. For instance, LLZO requires sintering at high temperatures (1100 – 1200 ^oC) and under high pressures (50 – 100 MPa) to achieve acceptable performance [6, 12]. These traditional ceramic manufacturing based on cumbersome processes like shape-forming and high-temperature sintering raise concerns over cost-effectiveness of oxide SEs. Furthermore, achieving a dense ceramic membrane with a desired level of thickness and uniformity for optimal conductivity and volumetric energy density remains a significant challenge. To compete with conventional Li-ion batteries that use polymer membrane separators, ceramic membranes need to have thicknesses around 20 μm [13]. Therefore, there is a pressing need for the development of new advanced processing techniques to manufacture thin ceramic SE membranes for ASSBs.

Several methods exist to fabricate thin ceramic layers suitable for large-scale production. These methods can be categorized based on the input material into three main groups: suspension, gas phase, or powder spray. Suspension-based methods, which include tape casting, screen printing, and roller coating, are well-established and offer scalability with a roll-to-roll production [14, 15]. However, they often require meticulous process control over factors such as suspension rheology, binder removal, and high temperature sintering to achieve the desired membrane density and uniformity. This challenge becomes even more pronounced when manufacturing LLZO membranes with thickness below 100 μm. Gas phase methods, exemplified by chemical vapor deposition (CVD), provide excellent uniformity even on rough surfaces. However, they come with their own set of challenges, including slow film growth rates and the use of potentially hazardous CVD source materials [16]. Gas phase methods also often necessitate post-sintering under controlled conditions.

In contrast, aerosol deposition (AD), which involves the high-speed spraying of ceramic powders, stands out as a cost-effective and scalable method that can form a dense ceramic membrane at room temperature [17, 18]. It allows for the direct construction of membranes with various thicknesses ranging from 1 μm to 100 μm by spraying ceramic particles onto substrate. The room temperature densification in AD is generally believed to occur through the fracture and plastic deformation of the ceramic particles within the film as they undergo high-speed collisions with the substrate (impact consolidation) [19, 20]. AD holds promise because it is not influenced by substrate shape and can be used to fabricate various film forms according to cell design. Moreover, AD eliminates the need for binders or additives. Since powder consolidation is achieved through impact energy without the need for additional heat or pressure, AD offers substantial flexibility in selecting starting powders. The method's adaptability, along with its capability to deposit films of varying thicknesses without binders, additives, and high-temperature sintering, renders it an attractive choice.

Beginning in 2007, several studies have explored the application of AD in battery technology [21, 22]. Investigations have covered anode materials such as $Li_4Ti_5O_{12}$ (LTO), graphite, and Si, as well as cathode materials like $LiCoO_2$ (LCO), $LiNi_{1/3}Co_{1/3}Mn_{1/3}O_2$ (NMC), and $LiFePO_4$ (LFP) [23-28]. The AD fabrication of an Al-LLZO solid electrolyte membrane was first reported in 2014 by Ahn et al., showcasing the potential for all-solid-state batteries (ASSBs) [26, 29]. However, the resulting Al-LLZO film exhibited low ionic conductivity, reaching only 1.0 x 10^{-8} S cm^{-1} even at 140 °C, along with poor cycle stability (see Table 1). Subsequent studies aimed to enhance Al-LLZO film conductivity. Hanft et al. achieved an improvement in effective film conductivity from 2.0 x 10^{-7} S cm^{-1} to 7.0 x 10^{-5} S cm^{-1} through post annealing at 600 °C [30]. Nazarenus et al. demonstrated decent symmetric cell cycle stability of up to 178 cycles at 70 °C with a current density of 1000 μA cm^{-2} [31]. However, the method is still in its early stage of development and requires further systematic studies to understand the correlation between starting particle properties, processing parameters, and deposited film characteristics.

As detailed in Table 2, numerous parameters significantly affect the AD process and the property of the final product film. While prior studies predominantly focused on aspects like impact velocity, nozzle-substrate distance, and gas pressure [17], in this study, we identified the morphology and size distribution of spraying particles as pivotal factors in the AD of Al-LLZO membrane to achieve the stable growth of a dense, high-performance SE membrane.

2. Experimental

2.1. Powder preparation

Two types of Al-doped LLZO ($Li_{6.25}Al_{0.25}La_3Zr_2O_{12}$, Al-LLZO) commercial powders were purchased from MSE supplies. The "sub-micron" (D50 < 600 nm) and "micron" (D50 <10 μm) commercial products were used as-received for the AD experiments. To obtain particles with intermediate sizes, the "micron" powders were subjected to ball milling using dry milling media (zirconia balls, Ø = 5 mm) in a planetary milling machine (PM200, Retsch). This milling process was carried out for 2 hours at 400 rpm, resulting in the "ball-milled micron" powder (D50 < 3 μm), which was also used for the AD experiment. The morphology of the powders was analyzed through scanning electron microscopy (SEM) using JEOL JCM-6000 PLUS microscope, and the particle size distribution was determined using ImageJ software. The phase purity of the Al-LLZO powders was assessed using X-ray diffraction (XRD) with Rigaku Miniflex instrument (Cu-Kα X-ray source, λ = 1.5406 Å).

2.2. Aerosol deposition experiments

Al-LLZO films were fabricated using an in-house built aerosol deposition (AD) system. Figure 1 illustrates the schematic diagram of the AD system, primarily composed of two chambers: the aerosol chamber and the deposition chamber. In the aerosol chamber, aerosols containing the powders to be deposited are generated through vibration. Subsequently, the aerosolized powders are transported into the deposition chamber through a nozzle. The acceleration of aerosols is achieved through a combination of pressure differences between the two chambers and the flow of an inert carrier gas. The accelerated aerosol powders are then consolidated onto a substrate through physical impact at a high speed, typically around 150 m s^{-1} [17]. A substrate is secured on an x-y-z linear stage, which enables precise control over the dimensions of the deposited area and the distance between the substrate and the nozzle.

The experimental parameters for the AD process are summarized in Table 2. Two chambers are required for AD deposition which are the deposition chamber and the aerosol chamber. Particles are accelerated by the pressure differences between aerosol chamber and deposition chamber. Digital pressure gauges are placed in both chambers, and in the deposition chamber, a pump is connected to maintain a high vacuum state. The deposition chamber had a pressure of 2 – 5 Torr while the aerosol chamber had a pressure of 100 – 300 Torr in this experiment aimed at optimizing Al-LLZO aerosol deposition. A commercially available aerosol generator (3400A, TSI Inc.) was used for Al-LLZO powder loading. The powder feed rate range is 180 to 1800 mg h^{-1}. Carrier gases such as helium (He) or nitrogen (N_2) were employed to accelerate the particles. The nozzle's moving speed was set at 0.06 m/s, and the scanning number was varied from 1 to 80. For substrate material, glass plate were used for initial screening, and silicon (Si) wafers were utilized for SEM analysis of the surface and cross-sectional morphologies. The Au interdigitated electrodes (IDEs, Metrohm, glass substrate, 10 μm width and digit length of 6760 μm) were also employed as a substrate for the film conductivity measurement. The size of the IDE was 2.29 cm x 0.76 cm x 0.07 cm. The position of the substrate was accurately controlled using an XYZ manipulator. All aerosol-deposited films were characterized in their as-deposited state, without any additional processes.

2.3. Property evaluation

The Al-LLZO films fabricated using the AD method underwent X-ray diffraction (XRD) and scanning electron microscopy (SEM) analysis to examine changes in crystal structure and morphology during deposition. Electrochemical impedance spectroscopy (EIS) measurements on films prepared on interdigitated electrodes (IDEs) were conducted at room temperature in the frequency range of 10 MHz to 1 Hz with 10 mV of AC perturbation, using an electrochemical workstation (VSP 300, BioLogic). The effective film conductivity (σ_{eff}) was calcualted by using the following equation:

$$\sigma_{\mathrm{eff}} = \frac{\mathrm{d}}{\mathrm{R_{tot}} \cdot A} = \frac{\mathrm{d}}{\mathrm{R_{tot}} \cdot l \cdot t}$$

where R_{tot} represents total resistance, *A* corresponds to the cross-sectional area of the film between IDE fingers, *t* represents the film thickness, *l* represents the IDE finger length (6760 µm), and d corresponds to the IDE finger spacing (10 µm) [30, 32].

3. Results and Discussion

3.1. Aerosol deposition of commercial Al-LLZO powders

Aerosol deposition experiments were conducted using commercially available Al-doped LLZO solid electrolyte powders having two distinct size distribution: “sub-micron” and “micron” grades. The XRD pattern of the “sub-micron” Al-LLZO powder aligned with the reference peaks of cubic-$Li_{6.25}Al_{0.25}La_3Zr_2O_{12}$ phase (JCPDS #80-0457), except for one peak that could be attributed to the $La_2Zr_2O_7$ minor impurity (Fig. S1, Supporting Information). The SEM image

(Figure 2a) revealed a mixture of small individual and large aggregated particles, with the primary particle sizes within the range of 400 – 600 nm. This "sub-micron" powder underwent aerosol deposition on glass slide substrates, and the resulting Al-LLZO film is shown in Figure 2b. The deposited surface appeared rough, uneven, and flawed. When subjected to a simple pen scratch test, the film exhibited poor adhesion (Fig. S2a, Supporting Information). This lack of consolidation and adhesion could be rationalized with insufficient mass of the "sub-micron" particles and corresponding inadequate kinetic energy during the deposition process. The low kinetic energy could cause sub-micron particles to rebound elastically rather than to undergo fracture – plastic deformation – adhesion processes. This suggested that the "sub-micron" sized particles may be too small to accumulate the requisite energy for effective impact consolidation [20].

An alternative attempt was made using "micron" sized Al-LLZO powder. The XRD pattern validated its cubic garnet structure without a detectable secondary phase (Fig. S1, Supporting Information). Figure 2c illustrates the more uniform size distribution (D50 < 10 μm) and morphology of the powder. The AD film produced from this "micron" Al-LLZO powder is shown in Figure 2d, where a 8 mm x 15 mm film layer was achieved after 30 AD scanning cycles, marking an enhancement in film quality compared to the previous attempt with "sub-micron" Al-LLZO powder. In Fig. S2b, the optical microscope image of the film deposited on a glass substrate exhibits a relatively dense and even surface morphology compared to that of the "sub-micron" AD film. Nevertheless, a non-uniform film thickness became evident upon an SEM examination of the film's cross section, as seen in Figure 2e.

Figure 2f represents the film's thickness trends relative to the number of AD scans. Initial scans, up to the 10^{th}, registered a linear correlation between film thickness and scan count. After this threshold, additional AD cycles did not result in a thicker film; the film growth stabilized between 10 and 50 scans, not surpassing ~7 μm. This saturation in growth could be explained with excessive kinetic energy of larger particles during aerosol deposition. In the initial 10 deposition cycles, the high impact energy of micron-sized particles likely facilitates film growth. Yet, in subsequent stages, this excessive kinetic energy may not solely contribute to film consolidation but also induce abrasive actions on the film's surface. Note that the non-uniform thickness observed in the "micron" Al-LLZO film could corroborate the abrasive "digging" of the film surface. Consequently, film growth stagnates once balance between consolidation and erosion is reached, which in this experiment was at approximately 7 μm. Summarizing the results from these aerosol deposition tests with both "sub-micron" and "micron" Al-LLZO powders, it can be inferred that the optimal particle size conducive to efficient AD film development may reside within the range of few micro-meters.

3.2. Particle size optimization for effective Al-LLZO film growth

To achieve the desired particle size, the "micron" sized Al-LLZO powder was subjected to modification using a high-energy ball milling process. Figure 3a displays the modified Al-LLZO particles, characterized by a uniform morphology with D50 < 3μm. XRD pattern (Figure 3d) of the ball-milled micron powder identified the emergence of minor secondary phases such as $La_2Zr_2O_7$ and $LaAlO_3$, which were likely due to the elevated temperatures encountered during high-energy ball milling [33]. Figure 3b and 3c present top-view and cross-sectional SEM images of the AD film formed with the processed Al-LLZO powder on a Pt-coated silicon (PtSi) substrate. The film's dense and uniform morphology distinctly underlined that adequate size and mass of powders required for effective impact consolidation and film growth were achieved with the ball-milling process (See also Fig. S2c for the dense film morphology deposited on a glass substrate). After 50 aerosol deposition scans, the film dimensions were registered as 8 mm x 14 mm, and its thickness measured ~24 µm. This thickness is comparable to the typical thickness (~20 µm) of polymer separators used in lithium-ion batteries.

Measuring the density of micron-thick films deposited on substrates presents significant challenges. While we couldn't directly measure the density of the AD film, the SEM morphology with no noticeable pores implies a high density for the "ball-milled micron" film. For comparative analysis, we prepared a high-temperature sintered pellet of Al-LLZO and compared its micro-morphology with the AD film. The SEM analysis of the sintered pellet sample reveals uniformly distributed multiple pores, approximately 1.8 µm in size (Figure S3, supporting information). Using the Archimedes method, we determined the density of this pellet sample to be 4.81 g cm^{-3}, corresponding to a relative sintering density of ~92.5 % (considering the theoretical density of LLZO is 5.2 g cm^{-3}). This comparison suggests that the relative density of our AD film is at least higher than 92.5 %.

Further insight into the structural fidelity of the aerosol deposited film was gleaned from XRD analysis. Figure 3d displays that Al-LLZO AD film was predominantly cubic-garnet Al-LLZO phase (Ia-3d). Additionally, trace of impurity phases, notably $La_2Zr_2O_7$, was observed. The origins of these impurities can be traced back to the ball-milled Al-LLZO powder. The consistent presence of these crystallographic phases from the input material to the film provided convincing evidence that the atomic structures remained unmodified during the aerosol deposition process.

Elaborating on the implications of particle size, Figure 4 illustrates how particle size influences effective Al-LLZO film fabrication. In the case of minuscule particles, their inadequate kinetic energy hindered film formation. Conversely, the use of larger particles (> ~10 µm) resulted in film erosion, constraining the film's growth below a certain thickness. However, with the introduction of medium-sized particles (~3 μm), optimal kinetic energy was achieved, leading to the formation of a dense Al-LLZO film. It is surmised that the effective growth of the AD film is intricately linked to the interplay between particle size and other factors, such as pressure difference and nozzle characteristics, all of which impact on kinetic energy of spraying powders.

3.3. Conductivity measurement of the Al-LLZO film

To assess the ionic conductivity of the Al-LLZO film fabricated with the ball-milled powder, electrochemical impedance spectroscopy (EIS) measurements were conducted. Figure 5 presents the Nyquist plots obtained from the EIS analysis performed at room temperature. Our Al-LLZO film demonstrated a decent in-plane conductivity of 1.18 x 10^{-5} S cm^{-1}. For context, as shown in Table 1, previous research on aerosol deposition of Al-LLZO films reported conductivity of 1 x 10^{-8} S cm^{-1} for as-deposited films [29], while ~10^{-5} S cm^{-1} was only achieved with post-annealing at temperatures exceeding 600 ºC [30]. The fact that our film reached this decent conductivity at its as-deposited state underscores the significance of particle size optimization.

In the development of practical ASSB cells, the area-specific resistance (R_A) value of the solid electrolyte component determines the overall cell performance. Impressively, our ~24 μm thick Al-LLZO film, crafted at room temperature, registers an R_A of 200 Ω cm^2. As a comparison, in order to match this R_A value, Al-LLZO thick films produced by high-temperature sintering techniques like tape casting (with a typical thickness of ~200 μm) and pellet pressing (a typical thickness of ~2 mm) would need ionic conductivities of 10^{-4} S cm^{-1} and 10^{-3} S cm^{-1}, respectively (Table 3). This highlights the potential of aerosol deposition as a promising and cost-effective method for producing solid electrolyte components with competitive performance metrics.

Achieving similar R_A values to conventionally sintered thicker SE membranes even with much lower ionic conductivities is a significant advantage that can pave the way for the development of high-performance All-Solid-State Batteries (ASSBs).

There exists the promising potential for further performance improvement of AD Al-LLZO, especially when juxtaposed with the ionic conductivity of ~10^{-4} S cm^{-1} typically achieved with conventional pellet pressing/sintering techniques [34]. Several factors might account for reduced ionic conductivity of our AD Al-LLZO. Firstly, the small grain size (i.e., large grain boundary fraction) could play a part. Although the AD technique employs particles of a few microns, these particles are fragmented upon impact and adhere to the substrate, possibly end up with finer grain sizes. Consequently, increased grain boundary resistance might hinder optimal ionic conductivity [35]. Another contributor could be the high interface resistance due to impurity phases. The AD experiments here were executed in a laboratory setting that, despite efforts to minimize, contains atmospheric moisture and CO_2. This environment might facilitate the incidental formation of minute LiOH or Li_2CO_3 impurities on the Al-LLZO powders' surface and interfaces. These could degrade the ionic conductivity, even though they remain undetected in XRD. Transitioning the experimental setup to a dry room and integrating post-annealing process could potentially improve the film's conductivity.

4. Conclusion

In this study, a dense and uniform Al-LLZO film, approximately 20 μm thick, was successfully fabricated using the aerosol deposition method at room temperature. The investigation underscored the significance of meticulously regulating particle size and morphology for achieving a high-quality AD membrane. Impressively, the film displayed an effective ionic conductivity of

~10^{-5} S cm^{-1}, achieved without the necessity for post-annealing. The observed ionic conductivity might be influenced by large grain-boundary fraction and potential impurity formation (such as LiOH and Li_2CO_3) during processing. For enhanced ionic conductivity, future efforts should delve into fine-tuning of film microstructure and its impact on transport properties. Potential pathways for improvement include post-annealing treatments and aerosol deposition in controlled atmosphere.

Declaration of competing interest

The authors declare that they have no known competing financial interests or personal relationships that could have appeared to influence the work reported in this paper.

Acknowledgement

This material is based upon work supported by Laboratory Directed Research and Development (LDRD) funding and Royalty funding from Argonne National Laboratory. Argonne is a U.S. Department of Energy laboratory managed by UChicago Argonne, LLC, under contract number DE-AC02-06CH11357. Part of the work performed by J.H. was supported by the Bisa Research Grant of Keimyung University in 2023 (Project No : 20230674).

References

[1] C. Sun, J. Liu, Y. Gong, D.P. Wilkinson, J. Zhang, Recent advances in all-solid-state rechargeable lithium batteries, Nano Energy 33 (2017) 363-386. https://doi.org/10.1016/j.nanoen.2017.01.028.

[2] D.Y. Oh, Y.E. Choi, D.H. Kim, Y.-G. Lee, B.-S. Kim, J. Park, H. Sohn, Y.S. Jung, All-solid-state lithium-ion batteries with TiS_2 nanosheets and sulphide solid electrolytes, Journal of Materials Chemistry A 4(26) (2016) 10329-10335. https://doi.org/10.1039/c6ta01628f.

[3] K.H. Park, Q. Bai, D.H. Kim, D.Y. Oh, Y. Zhu, Y. Mo, Y.S. Jung, Design strategies, practical considerations, and new solution processes of sulfide solid electrolytes for all-solid-state batteries, Advanced Energy Materials 8(18) (2018) 1800035. https://doi.org/10.1002/aenm.201800035.

[4] J. Ma, Y. Jiang, W. Chen, C. Luo, L. Zhang, H. Xu, J. Chang, W. Huang, C. Wang, S.-S. Chi, A low-cost Al-doped garnet $Li_7La_3Zr_2O_{12}$ with high ionic conductivity for high-energy solid-state lithium metal batteries, Applied Physics Letters 121(19) (2022) 193901. https://doi.org/10.1063/5.0123632.

[5] C. Wang, K. Fu, S.P. Kammampata, D.W. McOwen, A.J. Samson, L. Zhang, G.T. Hitz, A.M. Nolan, E.D. Wachsman, Y. Mo, Garnet-type solid-state electrolytes: materials, interfaces, and batteries, Chemical reviews 120(10) (2020) 4257-4300. https://doi.org/10.1021/acs.chemrev.9b00427.

[6] Y. Li, Z. Wang, C. Li, Y. Cao, X. Guo, Densification and ionic-conduction improvement of lithium garnet solid electrolytes by flowing oxygen sintering, Journal of Power Sources 248 (2014) 642-646. https://doi.org/10.1016/j.jpowsour.2013.09.140.

[7] H. Duan, H. Zheng, Y. Zhou, B. Xu, H. Liu, Stability of garnet-type Li ion conductors: An overview, Solid State Ionics 318 (2018) 45-53. https://doi.org/10.1016/j.ssi.2017.09.018.

[8] S. Abouali, C.-H. Yim, A. Merati, Y. Abu-Lebdeh, V. Thangadurai, Garnet-based solid-state Li batteries: from materials design to battery architecture, ACS Energy Letters 6(5) (2021) 1920-1941. https://doi.org/10.1021/acsenergylett.1c00401.

[9] M. Du, K. Liao, Q. Lu, Z. Shao, Recent advances in the interface engineering of solid-state Li-ion batteries with artificial buffer layers: challenges, materials, construction, and characterization, Energy & Environmental Science 12(6) (2019) 1780-1804. https://doi.org/10.1039/C9EE00515C.

[10] C. Guo, Y. Shen, P. Mao, K. Liao, M. Du, R. Ran, W. Zhou, Z. Shao, Grafting of lithiophilic and electron-blocking interlayer for garnet-based solid-state Li metal batteries via one-step anhydrous poly-phosphoric acid post-treatment, Advanced Functional Materials 33(10) (2023) 2213443. https://doi.org/10.1002/adfm.202213443.

[11] M. Du, Y. Sun, B. Liu, B. Chen, K. Liao, R. Ran, R. Cai, W. Zhou, Z. Shao, Smart construction of an intimate lithium garnet interface for all-solid-state batteries by tuning the tension of molten lithium, Advanced Functional Materials 31(31) (2021) 2101556. https://doi.org/10.1002/adfm.202101556.

[12] S. Yu, R.D. Schmidt, R. Garcia-Mendez, E. Herbert, N.J. Dudney, J.B. Wolfenstine, J. Sakamoto, D.J. Siegel, Elastic properties of the solid electrolyte $Li_7La_3Zr_2O_{12}$(LLZO), Chemistry of Materials 28(1) (2015) 197-206. https://doi.org/10.1021/acs.chemmater.5b03854.

[13] M. Balaish, J.C. Gonzalez-Rosillo, K.J. Kim, Y. Zhu, Z.D. Hood, J.L. Rupp, Processing thin but robust electrolytes for solid-state batteries, Nature Energy 6(3) (2021) 227-239. https://doi.org/10.1038/s41560-020-00759-5.

[14] J. Schnell, F. Tietz, C. Singer, A. Hofer, N. Billot, G. Reinhart, Prospects of production technologies and manufacturing costs of oxide-based all-solid-state lithium batteries, Energy & Environmental Science 12(6) (2019) 1818-1833. https://doi.org/10.1039/c8ee02692k.

[15] X. Xu, M. Luo, P. He, X. Guo, J. Yang, Screen printed graphene electrodes on textile for wearable electrocardiogram monitoring, Applied Physics A 125(10) (2019) 1-7. https://doi.org/10.1007/s00339-019-3006-x.

[16] J. Creighton, P. Ho, Introduction to chemical vapor deposition (CVD), Chemical vapor deposition 2 (2001) 1-22.

[17] J. Akedo, Aerosol deposition of ceramic thick films at room temperature: Densification mechanism of ceramic layers, Journal of the American Ceramic Society 89(6) (2006) 1834-1839. https://doi.org/10.1111/j.1551-2916.2006.01030.x.

[18] M. Schubert, D. Hanft, T. Nazarenus, J. Exner, M. Schubert, P. Nieke, P. Glosse, N. Leupold, J. Kita, R. Moos, Powder aerosol deposition method — novel applications in the field of sensing and energy technology, Functional Materials Letters 12(05) (2019) 1930005. https://doi.org/10.1142/s1793604719300056.

[19] J. Akedo, Room temperature impact consolidation (RTIC) of fine ceramic powder by aerosol deposition method and applications to microdevices, Journal of Thermal Spray Technology 17

(2008) 181-198. https://doi.org/10.1007/s11666-008-9163-7.

[20] D. Hanft, J. Exner, M. Schubert, T. Stöcker, P. Fuierer, R. Moos, An overview of the aerosol deposition method: Process fundamentals and new trends in materials applications, J. Ceram. Sci. Technol 6(3) (2015) 147-182. https://doi.org/10.4416/JCST2015-00018.

[21] H. Sakaguchi, T. Toda, Y. Nagao, T. Esaka, Anode properties of lithium storage alloy electrodes prepared by gas-deposition, Electrochemical and Solid-State Letters 10(11) (2007) J146. https://doi.org/10.1149/1.2772409.

[22] H. Usui, H. Nishinami, T. Iida, H. Sakaguchi, Anode properties of Cu-coated Si thick film electrodes prepared by electroless deposition and gas-deposition, Electrochemistry 78(5) (2010) 329-331. https://doi.org/10.5796/electrochemistry.78.329.

[23] R. Inada, K. Shibukawa, C. Masada, Y. Nakanishi, Y. Sakurai, Characterization of as-deposited $Li_4Ti_5O_{12}$ thin film electrode prepared by aerosol deposition method, Journal of Power Sources 253 (2014) 181-186. https://doi.org/10.1016/j.jpowsour.2013.12.084.

[24] S. Iwasaki, T. Hamanaka, T. Yamakawa, W.C. West, K. Yamamoto, M. Motoyama, T. Hirayama, Y. Iriyama, Preparation of thick-film $LiNi_{1/3}Co_{1/3}Mn_{1/3}O_2$ electrodes by aerosol deposition and its application to all-solid-state batteries, Journal of Power Sources 272 (2014) 1086-1090. https://doi.org/10.1016/j.jpowsour.2014.09.038.

[25] I. Kim, T.-H. Nam, K.-W. Kim, J.-H. Ahn, D.-S. Park, C. Ahn, B.S. Chun, G. Wang, H.-J. Ahn, $LiNi_{0.4}Co_{0.3}Mn_{0.3}O_2$ thin film electrode by aerosol deposition, Nanoscale research letters 7(64) (2012) 1-6. https://doi.org/10.1186/1556-276X-7-64.

[26] C.-W. Ahn, J.-J. Choi, J. Ryu, B.-D. Hahn, J.-W. Kim, W.-H. Yoon, J.-H. Choi, J.-S. Lee, D.-S. Park, Electrochemical properties of $Li_7La_3Zr_2O_{12}$-based solid state battery, Journal of Power Sources 272 (2014) 554-558. https://doi.org/10.1016/j.jpowsour.2014.08.110.

[27] I. Kim, J. Park, T.-H. Nam, K.-W. Kim, J.-H. Ahn, D.-S. Park, C. Ahn, G. Wang, H.-J. Ahn, Electrochemical properties of an as-deposited $LiFePO_4$ thin film electrode prepared by aerosol deposition, Journal of Power Sources 244 (2013) 646-651. https://doi.org/10.1016/j.jpowsour.2012.12.108.

[28] C.-W. Ahn, J.-J. Choi, J. Ryu, B.-D. Hahn, J.-W. Kim, W.-H. Yoon, J.-H. Choi, D.-S. Park, Microstructure and electrochemical properties of graphite and C-coated $LiFePO_4$ films fabricated by aerosol deposition method for Li ion battery, Carbon 82 (2015) 135-142. https://doi.org/10.1016/j.carbon.2014.10.043.

[29] C.-W. Ahn, J.-J. Choi, J. Ryu, B.-D. Hahn, J.-W. Kim, W.-H. Yoon, J.-H. Choi, D.-S. Park, Microstructure and ionic conductivity in $Li_7La_3Zr_2O_{12}$ film prepared by aerosol deposition method, Journal of the Electrochemical Society 162(1) (2014) A60. https://dor.org/10.1149/2.0411501jes.

[30] D. Hanft, J. Exner, R. Moos, Thick-films of garnet-type lithium ion conductor prepared by the aerosol deposition method: the role of morphology and annealing treatment on the ionic conductivity, Journal of Power Sources 361 (2017) 61-69. https://doi.org/10.1016/j.jpowsour.2017.06.061.

[31] T. Nazarenus, Y. Sun, J. Exner, J. Kita, R. Moos, Powder aerosol deposition as a method to produce garnet-type solid ceramic electrolytes: A study on electrochemical film properties and industrial applications, Energy Technology 9(7) (2021) 2100211. https://doi.org/10.1002/ente.202100211.

[32] J.H. Shu, H.C. Wikle, B.A. Chin, Passive chemiresistor sensor based on iron (II) phthalocyanine thin films for monitoring of nitrogen dioxide, Sensors and Actuators B: Chemical 148(2) (2010) 498-503. https://doi.org/10.1016/j.snb.2010.05.017.

[33] W. Cao, Synthesis of nanomaterials by high energy ball milling, Skyspring Nanomaterials, Inc (2007).

[34] W. Xia, B. Xu, H. Duan, Y. Guo, H. Kang, H. Li, H. Liu, Ionic conductivity and air stability of Al-doped $Li_7La_3Zr_2O_{12}$ sintered in alumina and Pt crucibles, ACS Appl Mater Interfaces 8(8) (2016) 5335-42. https://doi.org/10.1021/acsami.5b12186.

[35] M. Martin, Grain boundary ionic conductivity of yttrium stabilized zirconia as a function of silica content and grain size, Solid State Ionics 161(1-2) (2003) 67-79. https://doi.org/10.1016/s0167-2738(03)00265-0.

Table 1. Summary of previously reported studies for the aerosol deposition of Al-LLZO solid-electrolyte films.

Year	2015	2017		2021	**2023**
Material	Al_2O_3-added $Li_7La_3Zr_2O_{12}$	$Li_{5.3}Al_{0.4}La_3Zr_{1.5}Ta_{0.5}O_{12}$		$Li_{6.025}Al_{0.2}La_3Zr_{1.625}Ta_{0.375}O_{12}$	$\mathbf{Li_{6.25}Al_{0.25}La_3Zr_2O_{12}}$
Ionic conductivity [S cm^{-1}]	$1 \cdot 10^{-8}$ @ 140 °C	$2 \cdot 10^{-7}$ @ RT	$7 \cdot 10^{-5}$ @ RT	$4.7 \cdot 10^{-5}$ @ RT / $3.1 \cdot 10^{-4}$ @ 70 °C	**$1.18 \cdot 10^{-5}$ @ RT**
Post annealing treatment	No	No	Yes	Yes	**No**
Particle size	Micron	Submicron to micron		Micron	**Submicron to micron**
Pressure in deposition chamber	Not available	Not available		Not available	**2 – 5 Torr**
Gas flow rate	Not available	4 L/min		8 L/min	**1 -10 L/min**
Ref.	[29]	[30]		[31]	**This work**

Table 2. Summary of several parameters for AD experiment.

Parameters	Values
Carrier gas type	He or N_2
Gas flow rate	1 – 10 L/min
Substrates	Glass plate for initial screening, Si wafer for SEM analysis, IDE for EIS measurement
Additional substrate heating	None
Pressure in deposition chamber	2 – 5 Torr
Pressure in aerosol chamber	~100 – 300 Torr
Nozzle moving speed	0.06 mm/s
Scanning number	1- 80
Materials	Commercial $Li_{6.25}Al_{0.25}La_3Zr_2O_{12}$
Particle sizes	Sub-micron to micron size

Table 3. Comparison of area-specific resistance and required ionic conductivities of typical Al-LLZO membranes made by different methods.

Properties	**Aerosol deposition (This work)**	**Tape casting**	**Pellet pressing**
Densification condition	RT	>1000 ºC	>1000 ºC (with applied pressure)
Typical Thickness, L	20 μm	200 μm	2 mm
Area-specific resistance, R_A [Ω cm^2]	200	200	200
Required ionic conductivity, σ [S cm^{-1}]	$1 \cdot 10^{-5}$	$1 \cdot 10^{-4}$	$1 \cdot 10^{-3}$

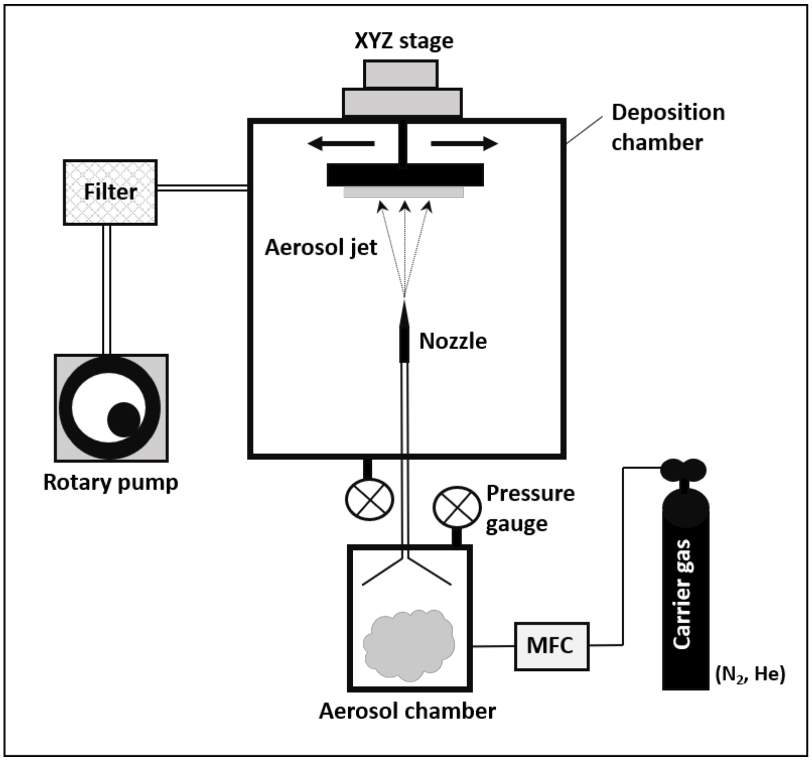

Figure 1. Schematic diagram of the Aerosol Deposition (AD) setup.

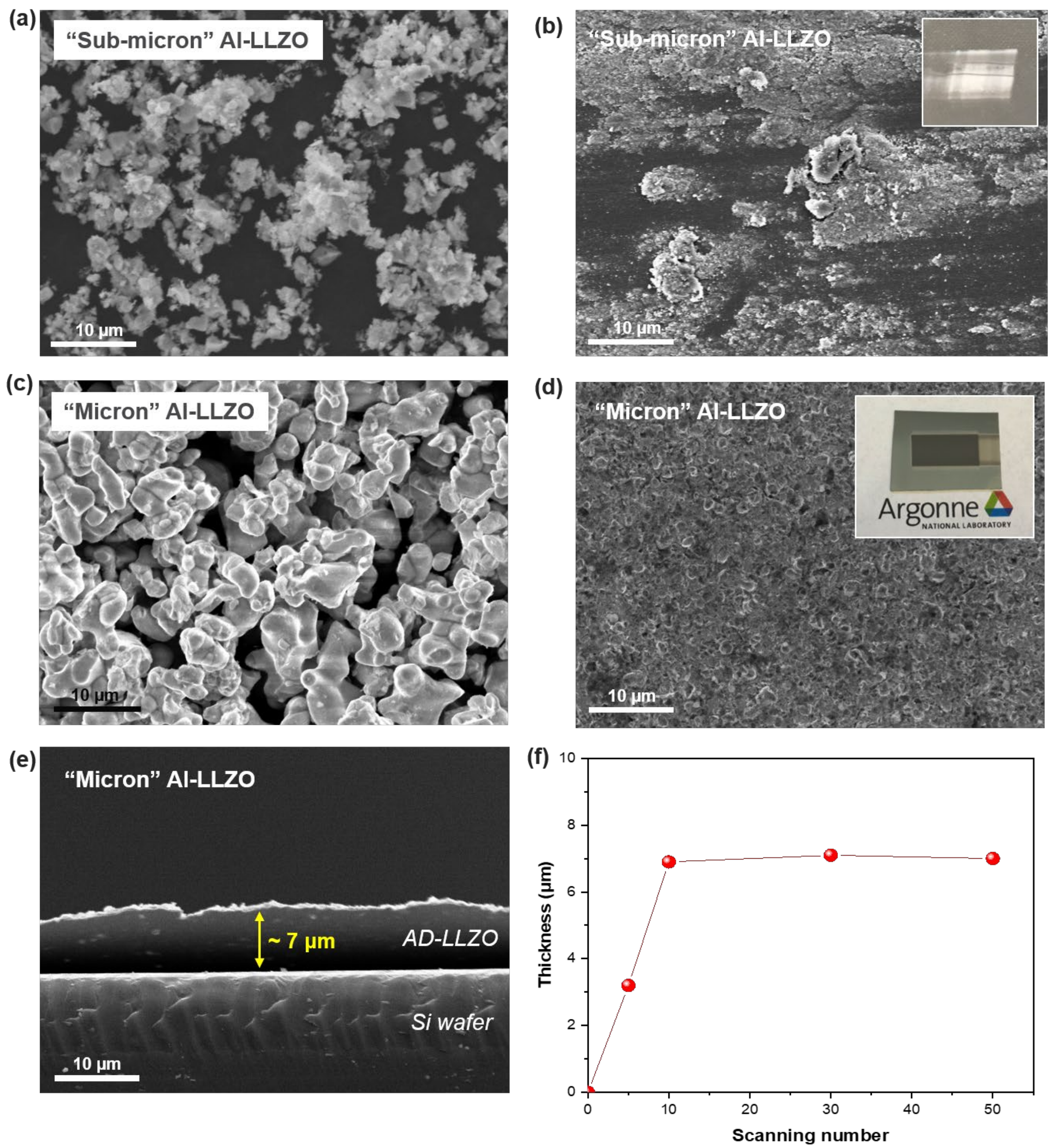

Figure 2. (a) SEM image of "sub-micron" Al-LLZO powder and (b) top-view SEM image of the Al-LLZO AD film fabricated with "sub-micron" Al-LLZO powder, (Inset shows photograph of the AD film); (c) SEM image of "micron" Al-LLZO powder, (d) top-view and (e) cross-sectional SEM images of the Al-LLZO AD film fabricated with "micron" Al-LLZO powder, (Inset of (d) shows photograph of the AD film), (f) film thickness as a function of AD scanning number.

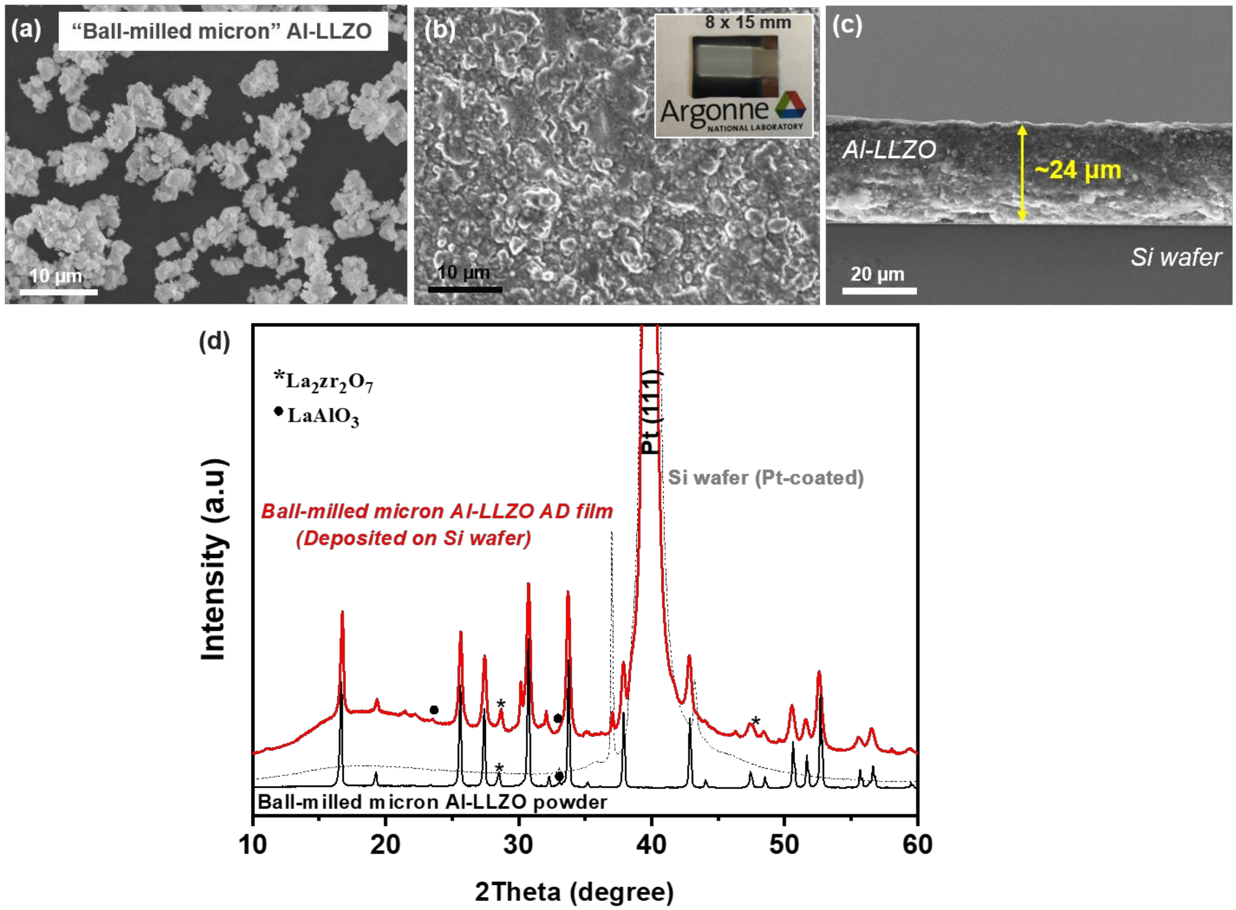

Figure 3. (a) SEM image of "ball-milled micron" Al-LLZO powder. (b) Top view and (c) cross-section SEM images of "ball-milled micron" Al-LLZO AD film. (d) XRD pattern of "ball-milled micron" Al-LLZO powder and AD film.

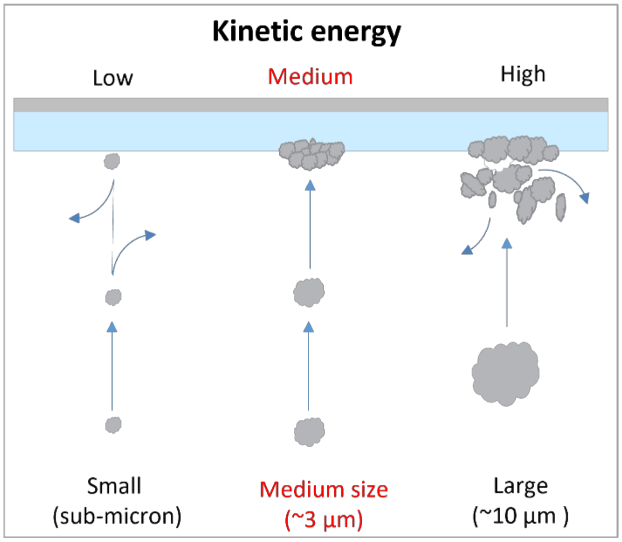

Particle size	Effect
Small (~400 nm)	• Low kinetic energy • Elastic bouncing • No film formation
Medium size (~3 µm)	• Medium kinetic energy • Plastic deformation • Impact consolidation and decent film formation
Large (~10 µm)	• High kinetic energy • Fracture of particles • Particle erosion • Film does not grow beyond a certain thickness

Figure 4. The schematic of particle size effects on the AD Al-LLZO film growth mechanism.

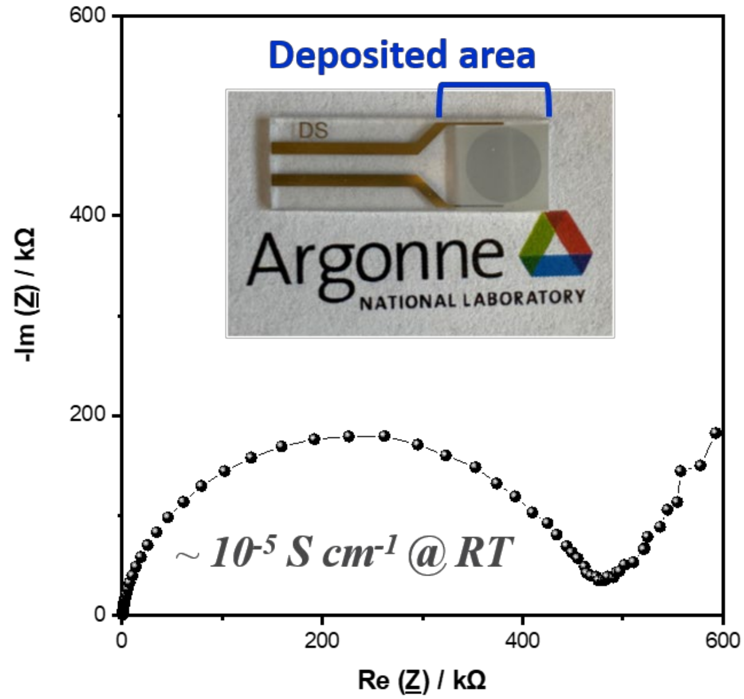

Figure 5. Impedance plot of ball-milled Al-LLZO AD film at room temperature; (inset) digital image of "ball-milled micron" Al-LLZO AD film deposited on an IDE electrode.